BMC Medical Imaging

RESEARCH

Open Access

Endoscopic ultrasonography-based intratumoral and peritumoral machine learning ultrasomics model for predicting the pathological grading of pancreatic neuroendocrine tumors

Shuangyang Mo[1,2†], Cheng Huang[3†], Yingwei Wang[1†] and Shanyu Qin[2*]

Abstract

Objectives The objective is to develop and validate intratumoral and peritumoral ultrasomics models utilizing endoscopic ultrasonography (EUS) to predict pathological grading in pancreatic neuroendocrine tumors (PNETs).

Methods Eighty-one patients, including 51 with grade 1 PNETs and 30 with grade 2/3 PNETs, were included in this retrospective study after confirmation through pathological examination. The patients were randomly allocated to the training or test group in a 6:4 ratio. Univariate and multivariate logistic regression were used for screening clinical and ultrasonic characteristics. Ultrasomics is ultrasound-based radiomics. Ultrasomics features were extracted from both the intratumoral and peritumoral regions of conventional EUS images. Subsequently, the dimensionality of these radiomics features was reduced using the least absolute shrinkage and selection operator (LASSO) algorithm. A machine learning algorithm, namely multilayer perception (MLP), was employed to construct prediction models using only the nonzero coefficient features and retained clinical features, respectively.

Results One hundred seven ultrasomics features based on EUS were extracted, and only features with nonzero coefficients were ultimately retained. Among all the models, the combined ultrasomics model achieved the greatest performance, with an AUC of 0.858 (95% CI, 0.7512 - 0.9642) in the training group and 0.842 (95% CI, 0.7061 - 0.9785) in the test group. A calibration curve and a decision curve analysis (DCA) also demonstrated its accuracy and utility.

Conclusions The integrated model using EUS ultrasomics features from intratumoral and peritumoral tumors accurately predicts PNETs' pathological grades pre-surgery, aiding personalized treatment planning.

Trial registration ChiCTR2400091906.

Keywords Pancreatic neuroendocrine tumors, Endoscopic ultrasonography, Ulstrasomics, Machine learning, Pathological grading

†Shuangyang Mo, Cheng Huang and Yingwei Wang are co-first authors.

*Correspondence:
Shanyu Qin
qinshanyu@gxmu.edu.cn
Full list of author information is available at the end of the article

Introduction

Pancreatic neuroendocrine tumors (PNETs) originate from neuroendocrine cells of the pancreas and are one type of neuroendocrine neoplasm (NEN), representing 3% of all pancreatic tumors [1, 2]. Although PNETs are relatively uncommon, their incidence is growing owing to the increased use of cross-sectional imaging [3, 4]. The 2022 World Health Organization (WHO) classifies PNETs into well-differentiated (grade 1, G1), intermediately differentiated (grade 2, G2), and poorly differentiated (grade 3, G3) tumors based on their mitotic rate and Ki-67 proliferation index [5]. Tumor grading is a critical prognostic indicator for individuals with PNETs [6, 7]. PNETs demonstrate a diverse spectrum of biological behavior, ranging from low-grade malignancy (G1) to highly aggressive (G3) tumors [8]. G1 asymptomatic and non-functional PNETs, especially those with a diameter smaller than 2 cm, are recommended to undergo active monitoring [9]. Conversely, prior research has suggested that G2 non-functional PNETs should be categorized as high-risk and G2/3 PNETs are associated with poorer prognoses and typically necessitate more aggressive treatment [10–12]. Due to the significant influence of pathological grading on treatment strategies, accurate determination of PNETs grading is crucial in clinical settings to ensure optimal patient therapies [13].

Nowadays, surgical removal of tumors serves as the mainstay of treatment for the majority of PNETs, particularly for the G2/3 ones [14, 15]. The most reliable approach for the pathological grading of PNETs continues to be the examination of postoperative pathological specimens [16], highlighting the limitations of preoperative prognostic stratification methods [17]. Presently, the primary method for preoperative diagnosis and grading of PNETs is endoscopic ultrasonography-guided fine-needle aspiration/biopsy (EUS-FNA/B) [18–20]. Nevertheless, this technique is hindered by its invasiveness, limited accuracy, challenges in capturing tumor heterogeneity, and a high technical threshold [21]. Hence, there is a pressing need for a precise and non-invasive technique to identify and classify G1 and G2/3 PNETs before surgical intervention.

Previous studies have shown that computed tomography (CT), magnetic resonance imaging (MRI), and EUS can help predict the grading of PNETs before surgery [22–29], but their accuracy and validation may hard to accomplish the diagnostic requirements [3, 30]. EUS is commonly used to diagnose PNETs and is considered a highly accurate imaging tool for pancreatic diseases due to its ability to produce detailed images of pancreatic lesions [31]. According to European Neuroendocrine Tumor Society (ENETS) guidelines, EUS is the preferred imaging method when other tests are inconclusive [32]. EUS has demonstrated superior efficacy in the detection of PNETs compared to CT, MRI, and abdominal ultrasonography (US), especially for small lesions [33, 34].

Standardized imaging technology, big data analytics, artificial intelligence, and interpretable machine learning algorithms demonstrate significant potential in the realm of medical research [3, 35, 36]. Recently, the integration of radiomics and machine learning strategies as an emergent imaging analysis for tumor diagnosis, treatment evaluation, and prognosis assessment has been rapidly widespread [37, 38]. Numerous studies have shown that radiomic features in MR imaging can reflect tumor heterogeneity and predict glioma grading [39].

Radiomics techniques have also been effective in predicting the grading of PNETs on CT and MRI scans [40–42]. Additionally, features from ultrasomics analysis of B-mode ultrasound images show potential in predicting PNETs' pathological grading [43]. Additionally, prior research has demonstrated a significant association between radiomics features of the peritumoral region and tumor-related outcomes, including diagnostic accuracy, pathological characteristics, and prognostic indicators [44–46].

The effectiveness of ultrasomics approaches utilizing EUS in distinguishing between G2/3 and G1 PNETs remains uncertain, despite the acknowledged superiority of EUS as an imaging modality. Leveraging existing knowledge, we employed a machine learning algorithm to construct and validate a robust ultrasomics model incorporating intratumoral and peritumoral characteristics, intending to accurately predict the pathological grading of PNETs. Concurrently, we integrated the models with Shapley Additive Explanations (SHAP) to elucidate and visualize the model outputs.

Materials and methods

Study population

This retrospective study was approved by the institutional ethics review board of the First Affiliated Hospital of Guangxi Medical University (No. 2023-K346-01, 2023-12-29), which waived the need for patient approval or signed informed consent to review medical images and clinical information. This study included 81 patients with PNETs, 51 with G1 and 30 with G2/3, who had surgery or EUS-FNB at our institution from October 2013 to January 2024. The inclusion and exclusion criteria are displayed as follows.

Patients in the study had to meet specific criteria: they had to have a preoperative EUS scan of the pancreas, confirmation of PNETs and their grade through pathology, clear EUS images before biopsies, and no prior chemotherapy or radiotherapy. Patients excluded from the study did not meet criteria such as the inability to display the

entire lesion, motion artifacts or noise in images, and the presence of other tumors. Registered patients were randomly assigned to a training or test group in a 6:4 ratio. Figure 1 shows how the study population was enrolled for a retrospective analysis.

EUS image acquisition

A standard dynamic EUS procedure was applied based on the EU-ME2 device (Olympus, Japan) and the SU-9000 device (FUJIFILM, Japan). All the ESU images were consistently taken by an experienced EUS specialist, who has a track record of over 10000 EUS practices, resulting in high-quality images of pancreatic lesions. Images were standardized with a level of 125 and a window of 250 grayscale values, and stored in our institutional Picture Archiving and Communication System (PACS).

Endoscopic ultrasonography features and clinical characteristics

In this research, a retrospective analysis was conducted on various clinical parameters, including age, gender, and pathological diagnosis. To bolster the study's validity, all EUS images were thoroughly scrutinized and assessed by two skilled EUS specialists, each possessing 6-7 years of experience in pancreatic EUS. Importantly, these specialists were unaware of the histopathological and clinical information related to the cases under analysis. This study analyzed clinical parameters and endoscopic ultrasonography features of pancreatic masses, including age, gender, pathology grading, location of the pancreatic mass, maximum diameter, shape, margin characteristics, echo characteristics, uniformity of echo, calcification, and cystic. In cases of multiple pancreatic lesions, the analysis focused primarily on the largest lesion with confirmed pathology.

ROI delineation

Images were stored in Digital Imaging and Communications in Medicine (DICOM) format and converted to nii.gz format. Two experts in EUS, with 6 and 7 years of experience, manually delineated the intratumoral region of interest (ROI) utilizing ITK-SNAP software (version 3.8.1, website as http://www.itksnap.org). In instances of disagreement between the two specialists, a dialogue and consensus method were utilized. Both specialists were blinded to the pathological results. The lesions were segmented layer by layer along the edges on conventional EUS images, excluding neighboring normal tissue, blood vessels, bile ducts, and pancreatic ducts. Our prior research demonstrated that integrating EUS intratumoral features with radiomic features of the peritumoral region, extending 3 mm

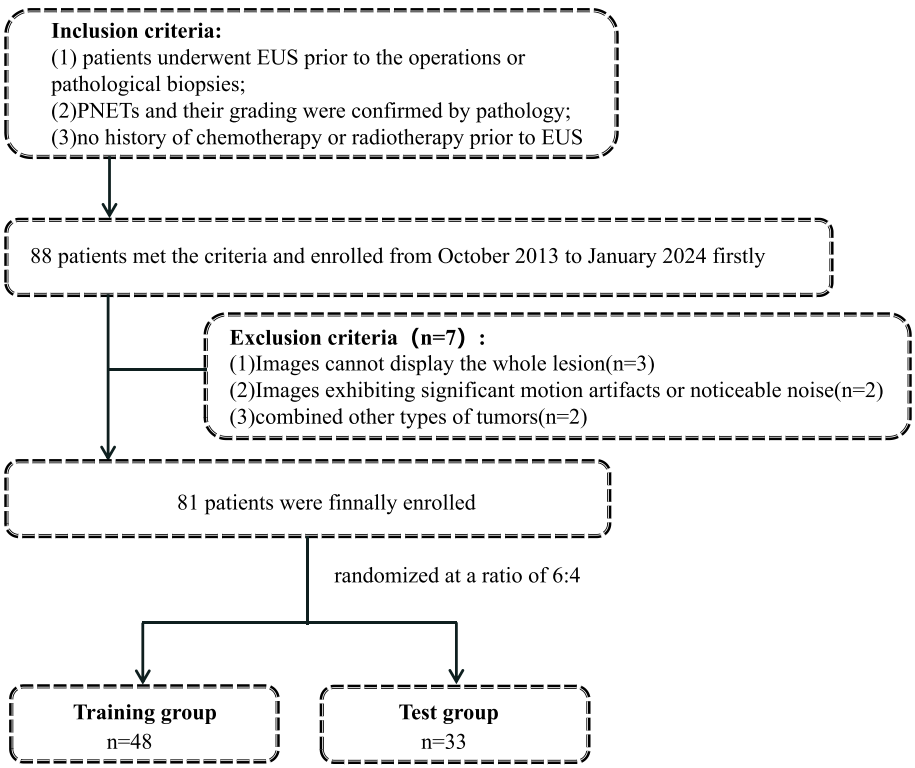

Fig. 1 Flowchart for enrolling the study population

outward enhanced the model's efficacy in distinguishing between insulinomas and nonfunctional PNETs [47]. However, it remains unclear whether the peritumoral region contains predictive and diagnostic information for grading PNETs. Given the mean tumor sizes of 28.21 ± 16.05 mm and 29.29 ± 19.25 mm in the training and test groups, respectively, a threshold of 3 mm was selected to prevent the inadvertent inclusion of extrapancreatic regions that do not contribute meaningful information. The peritumoral ROI was obtained through the utilization of a conventional morphological dilation technique within the ITK-SNAP software. This method entailed enlarging the delineation of the intratumoral ROI by 3 mm. All peritumoral ROIs were finally examined by an endoscopist. Following this, three separate ROI images were chosen for each EUS image, including an intratumoral ROI, a peritumoral ROI, and a combined ROI that encompassed both the intratumoral and peritumoral ROIs. A detailed depiction of the process for acquiring the ROIs can be found in Fig. 2.

Standardization techniques were utilized for image and data preprocessing to enhance the reproducibility of the results. The intraclass correlation coefficient (ICC) was used to assess the consistency among and within observers. A cohort of 25 patients, comprising 18 with G1 PNETs and 10 with G2/3 PNETs, was randomly chosen for the study. After two weeks, the EUS specialists segmented the ROIs again, using an ICC threshold of > 0.8 to signify a high level of agreement.

Ultrasomics feature extraction

The classification of handcrafted features can be divided into three distinct categories: geometric, intensity, and textural. Geometric features focus on the three-dimensional morphological attributes of tumors. Intensity features involve the statistical distribution of voxel intensities within the tumor in the first order. In contrast, textural features analyze patterns and higher-order spatial distributions of intensities. This study employed various methodologies, such as the gray level co-occurrence matrix (GLCM), gray level run length matrix (GLRLM), gray level size zone matrix (GLSZM), and neighborhood gray-level difference matrix (NGTDM), for the extraction of texture features from the region of interest (ROI). The ulstrasomics features were extracted from the intratumoral and peritumoral ROIs separately, and the features of the combined ROIs were obtained by integrating those extracted from both regions. The extraction processes followed the guidelines set forth by the Image Biomarker Standardization Initiative (IBSI).

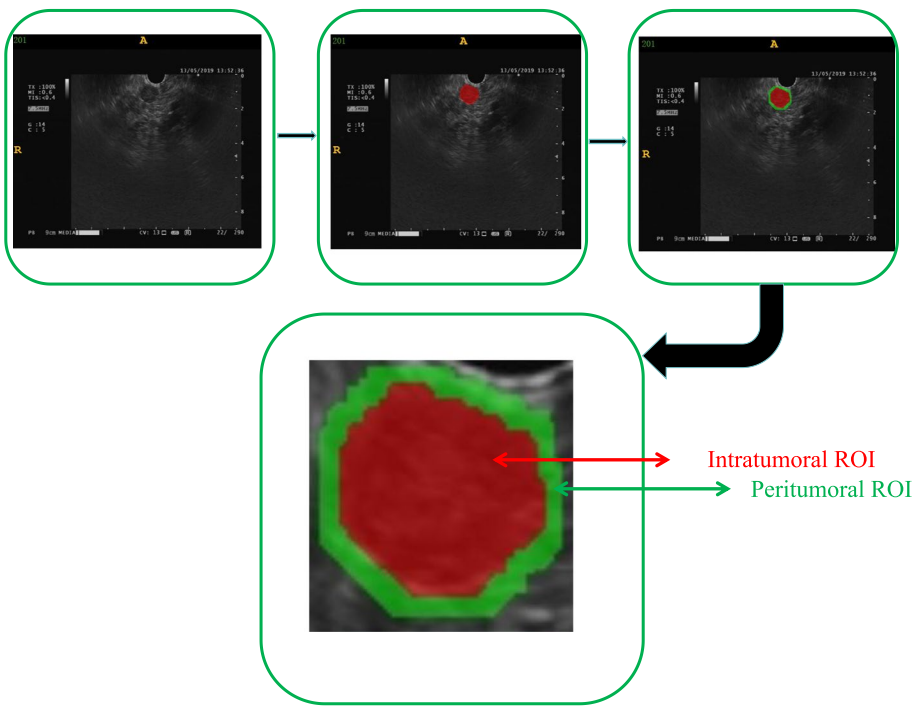

Fig. 2 Comprehensive graph of the intratumoral and peritumoral ROIs. The red region indicates the "intratumoral ROI"; the green region indicates the "peritumoral ROI". (ROI, region of interest)

Ultrasomics feature selection

A Mann-Whitney U test was conducted to compare features between the training and test groups. Ultrasomics features with a significance level of $p < 0.05$ were selected for subsequent analysis. Spearman's rank correlation coefficient was employed to assess the interrelationship among each ultrasomics feature, aiming to verify the features' reliability. Features exhibiting a correlation coefficient exceeding 0.9 with another feature were preserved with one of them. To improve feature representation, a greedy recursive deletion method was applied for feature filtering. This method entailed iteratively removing the feature with the highest level of redundancy within the existing set. The study employed the least absolute shrinkage and selection operator (LASSO) regression model to identify ultrasomics features with nonzero coefficients through the 10-fold cross-validation technique. Notably, the minimum criterion determined the penalty parameter (lambda.min). Feature selection was carried out in the training group and then applied to the test group. The LASSO regression analysis was performed using the Python scikit-learn package.

Ultrasomics features with non-zero coefficients were selected for inclusion in the regression model and combined to create an ultrasomics signature. Subsequently, each patient was assigned an ultrasomics score by applying a linear combination of the selected features and their respective model coefficients.

Construction of different ultrasomics models and clinical models

A Multilayer Perceptron (MLP) machine learning algorithm was employed to create classification models for the accurate differentiation of G1 and G2/3 PNETs. After applying LASSO feature selection, the chosen intratumoral ultrasomics features, peritumoral ultrasomics features, and combined ultrasomics features were utilized as inputs for MLP models to establish an intratumoral ultrasomics model, a peritumoral ultrasomics model, and a combined ultrasomics model. Additionally, a clinical model, based on MLP, was also constructed using selected endoscopic ultrasonography features. All these models were established definitively by utilizing a 5-fold cross-validation methodology. To achieve optimal model

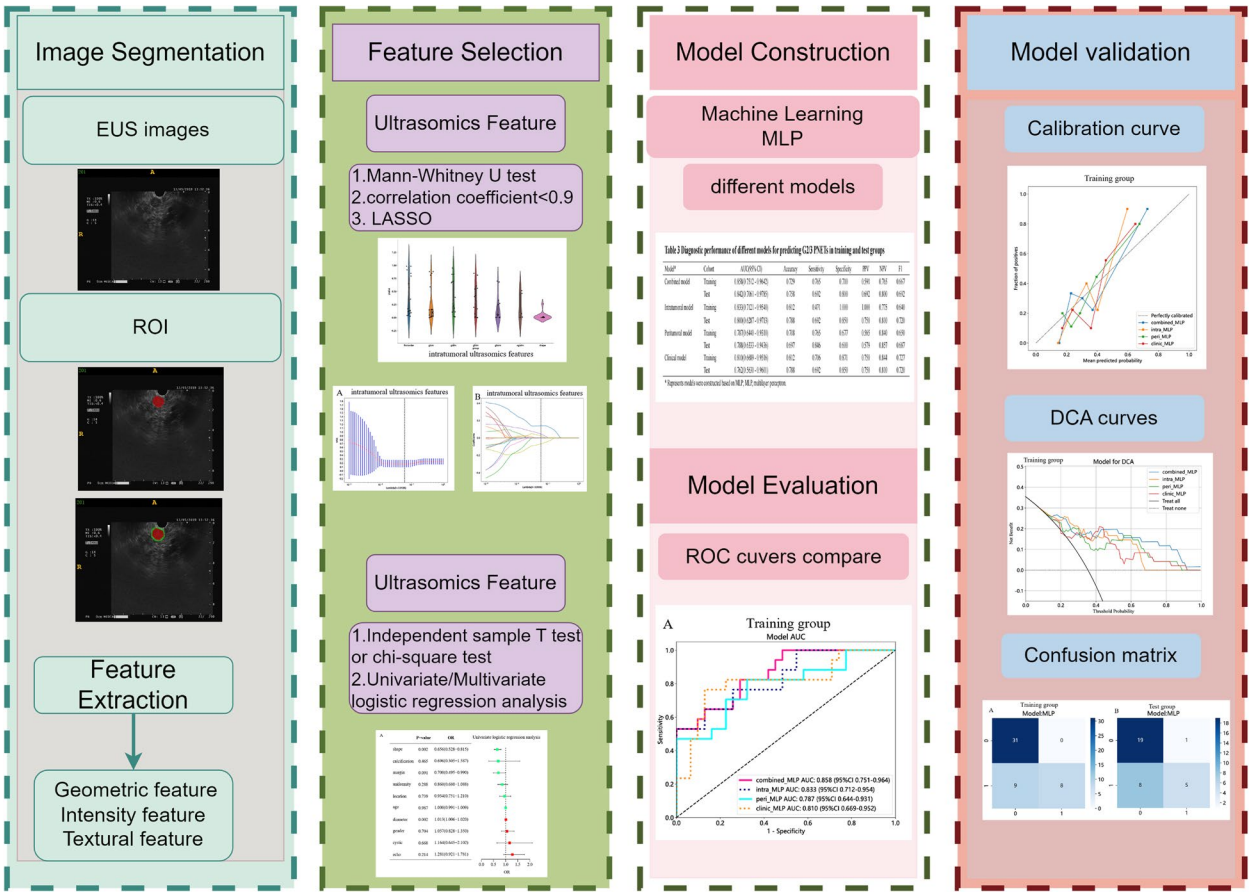

Fig. 3 The workflow of this study

performance and mitigate the risk of overfitting, we conducted hyperparameter tuning.

Ultrasomics models and clinical model assessment

The diagnostic effectiveness of various machine learning models was evaluated by assessing metrics including the receiver operator characteristic curve (ROC), area under the curve (AUC), accuracy, specificity, sensitivity, positive predictive value (PPV), F1 Score, and negative predictive value (NPV). Furthermore, a Delong test was employed to compare the performance of these ultrasomics and clinical models in terms of the AUC.

The alignment between the prognostic forecasts generated by diverse ultrasomics models, clinical model, and the resultant outcomes was assessed through the computation of the calibration curve, which juxtaposed the prognostic estimates of these models with the actual observations. The calibration performance of three ultrasomics models and one clinical model was evaluated by constructing calibration curves and using the Hosmer-Lemeshow (H-L) test to assess their calibration ability. Additionally, decision curve analysis (DCA) was employed to evaluate the clinical utility of these predictive models. Finally, the SHAP value of each retained ultrasomics feature was computed to enhance the interpretability of the predictions generated by the machine learning model.

Statistical analysis

The study compared the clinical parameters, endoscopic ultrasonography features, and ultrasomics features of patients using statistical tests including the independent sample t-test, Mann–Whitney U test, or X2 test. In addition, univariate and multivariate logistic regression were used to screen risk factors. A significance threshold of a two-tailed p-value < 0.05 was set. The prediction

Table 1 Clinical and radiological characteristics in the training and test groups

Variable	Training cohort ($N = 48$)			Test cohort ($N = 33$)		
	G1	G2/3	*P*-value	G1	G2/3	*P*-value
Age	50.87 ± 12.44	50.94 ± 15.96	0.597	41.60 ± 12.33	47.15 ± 13.74	0.276
Maximum diameter	23.13 ± 12.03	37.47 ± 18.55	0.005	23.17 ± 16.19	38.70 ± 20.38	0.022
Gender			0.938			0.478
0	20(64.52)	10(58.82)		13(65.00)	6(46.15)	
1	11(35.48)	7(41.18)		7(35.00)	7(53.85)	
Shape			0.007			0.047
0	8(25.81)	12(70.59)		3(15.00)	7(53.85)	
1	23(74.19)	5(29.41)		17(85.00)	6(46.15)	
Margin			0.210			0.012
0	2(6.45)	4(23.53)		0(0.00)	5(38.46)	
1	29(93.55)	13(76.47)		20(100.00)	8(61.54)	
Echo			0.402			0.398
0	6(19.35)	1(5.88)		3(15.00)	0(0.00)	
1	25(80.65)	16(94.12)		17(85.00)	13(100.00)	
Uniformity			0.434			0.146
0	15(48.39)	11(64.71)		9(45.00)	10(76.92)	
1	16(51.61)	6(35.29)		11(55.00)	3(23.08)	
Calcification			1.000			0.826
0	30(96.77)	17(100.00)		18(90.00)	7(53.85)	
1	1(3.23)	0(0.00)		2(10.00)	6(46.15)	
Cystic areas			1.000			0.051
0	30(96.77)	16(94.12)		18(90.00)	7(53.85)	
1	1(3.23)	1(5.88)		2(10.00)	6(46.15)	
Location			0.97			1.000
0	13(41.94)	8(47.06)		11(55.00)	7(53.85)	
1	18(58.06)	9(52.94)		9(45.00)	6(46.15)	

Gender: "0" means female, "1" means male; Shape: "0" means irregular shape, "1" means regular shape; Margin: "0" means unclear margin of lesion, "1" means clear margin of lesion; Echo: "0" means means not hypoechoic of lesion, "1" means hypoechoic of lesion; uniformity: "0" means nonuniformity of echo; "1" means uniformity of echo; Calcification: "0" means no calcification, "1" means calcification; Cystic areas: "0" means no cystic areas, "1" means cystic areas; Location: "0" means head and uncinate process of the pancreas, "1" means body and tail of the pancreas

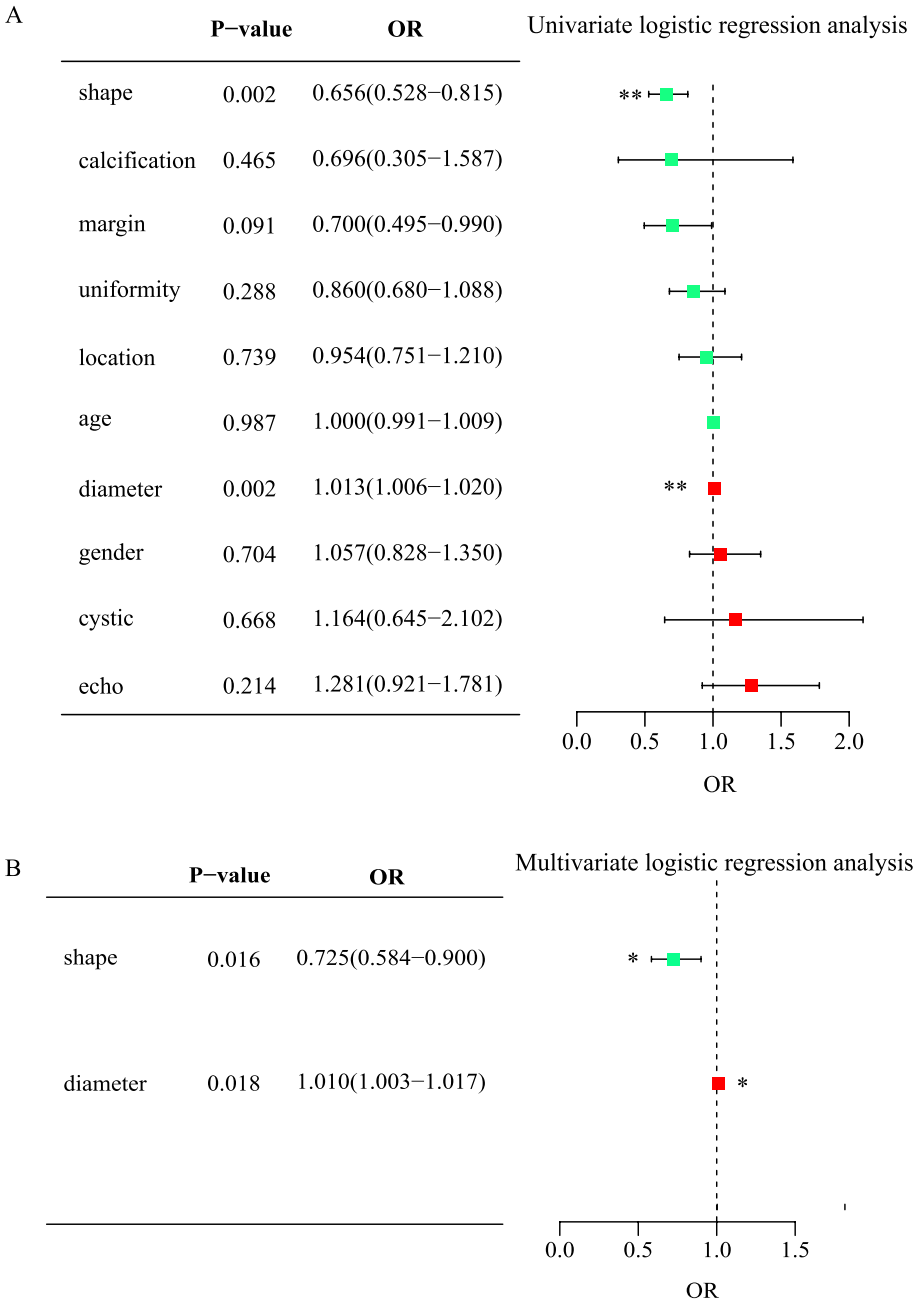

Fig. 4 **A** Forest map of univariate logistic regression of clinical and radiological characteristics; **B** Forest map of multivariate logistic regression of clinical and radiological characteristics. (* means *P*-value < 0.05; ** means *P*-value < 0.01)

performance of various models was assessed using metrics such as AUC, accuracy, sensitivity, specificity, PPV, F1 score, and NPV. A Delong test was used to compare AUC values between different models to evaluate their performance. The study workflow is depicted in Fig. 3.

Results

Baseline population characteristics and endoscopic ultrasonography features

In this retrospective study, a total of 81 patients (49 women, 32 men) were included, with 48 patients in the training group and 33 patients in the test group. The

results revealed no significant differences in age, gender, shape, echo characteristics, echo uniformity, calcification, mass location, and presence of cystic degeneration between patients with G1 and G2/3 PNETs in both the training and test groups. However, it was observed that G1 PNETs had a significantly smaller diameter and more regular shape compared to G2/3 PNETs (Table 1). Both univariate (Fig. 4A) and multivariate (Fig. 4B) logistic regression analyses indicated a significant association between maximum diameter (OR = 1.010, 95% CI 1.003–1.017) and shape (OR = 0.725, 95% CI 0.584–0.900) with G2/3 PNETs (Table 2).

Ultrasomics feature extraction and screening

The extraction and screening of radiomic features were conducted utilizing PyRadiomics, an internal feature analysis software, enabling the extraction of all manually crafted features. A comprehensive set of seven categories and 107 ultrasomics features were successfully obtained, comprising 18 first-order features, 14 shape features, and the remaining texture features. The definitions for these manually crafted features have been previously documented in prior literature [35].

The comprehensive series of intratumoral (Fig. 5A), peritumoral (Fig. 5B), and combined ultrasomics features (Fig. 5C), along with their corresponding *p* values, are presented in Fig. 5**.** Four intratumoral ultrasomics features with nonzero coefficients were retained following feature downsizing and LASSO logistic regression. The coefficients and mean standard errors (MSEs) obtained from the 10-fold validation are depicted in Fig. 6A and B, respectively. Additionally, Fig. 6C showcases the retained intratumoral ultrasomics features and their corresponding coefficients. Similarly, Fig. 6D, E, and F display six peritumoral ultrasomics features, while Fig. 6G, H, and I exhibit six combined ultrasomics features, all of which have nonzero coefficients. The linear expressions are presented in Supplementary materials. Finally, based on the MLP algorithm, these retained intratumoral, peritumoral, and combined ultrasomics features were applied to construct intratumoral, peritumoral, and combined ultrasomics models for predicting G2/3 PNETs, respectively.

The intratumoral, peritumoral, clinical, and combined ultrasomics models and their performance

Supplementary Fig. 1 presents the performance of various machine learning algorithms within intratumoral ultrasomics models. It is noteworthy that the Random Forest (RF), XGBoost, and ExtraTrees models exhibit tendencies toward overfitting. This issue is also observed in the Support Vector Machine (SVM) and LightGBM models, as evidenced by the higher AUC values in the testing group compared to the training group. In contrast, the MLP model demonstrates superior performance relative to the Logistic Regression (LR) and K-Nearest Neighbors (KNN) models. The MLP model shows greater consistency between the training group (AUC = 0.833, 95% CI: 0.712—0.954) and the test group (AUC = 0.800, 95% CI: 0.629—0.971), underscoring its potential as an optimal model for further analyses.

Subsequently, the variables of maximum diameter and shape, identified through univariate and multivariate logistic regression analyses, were selected for the development of a clinical model employing an MLP to predict G2/3 PNETs. This clinical model demonstrated an AUC = 0.810 (95% CI 0.6689 - 0.9516) in the training group, with an accuracy of 0.812, sensitivity of 0.706, specificity of 0.871, PPV of 0.750, and NPV of 0.844. Furthermore, in the test group, the clinical model achieved an AUC = 0.762 (95% CI 0.5630 - 0.9601) (Table 3).

The ROC curves and AUCs of the clinical model, and intratumoral, peritumoral, and combined ultrasomics models, generated using the MLP algorithm, are

Table 2 Univariate and multivariable logistic regression analyses for selecting clinical and radiological characteristics

Variable	Univariate analysis		Multivariate analysis	
	OR (95% CI)	*P*-value	OR(95% CI)	*P*-value
Age	1.000(0.991, 1.009)	0.987		
Maximum diameter	1.013(1.006, 1.020)	0.002**	0.725(0.584,0.900)	0.016*
Shape	0.656(0.528,0.815)	0.002**	1.010(1.003,1.017)	0.018*
Margin	0.700(0.495,0.990)	0.091		
Echo	1.281(0.921, 1.781)	0.214		
uniformity	0.860(0.680,1.088)	0.288		
Calcification	0.696(0.305,1.587)	0.456		
Cystic areas	1.164(0.645, 2.102)	0.668		
Location	1.109(0.996,1.236)	0.115		
Gender	1.057(0.828,1.350)	0.704		

OR Odds ratio, *CI* Confidence interval,* means *P*-value < 0.05, ** means *P*-value < 0.01

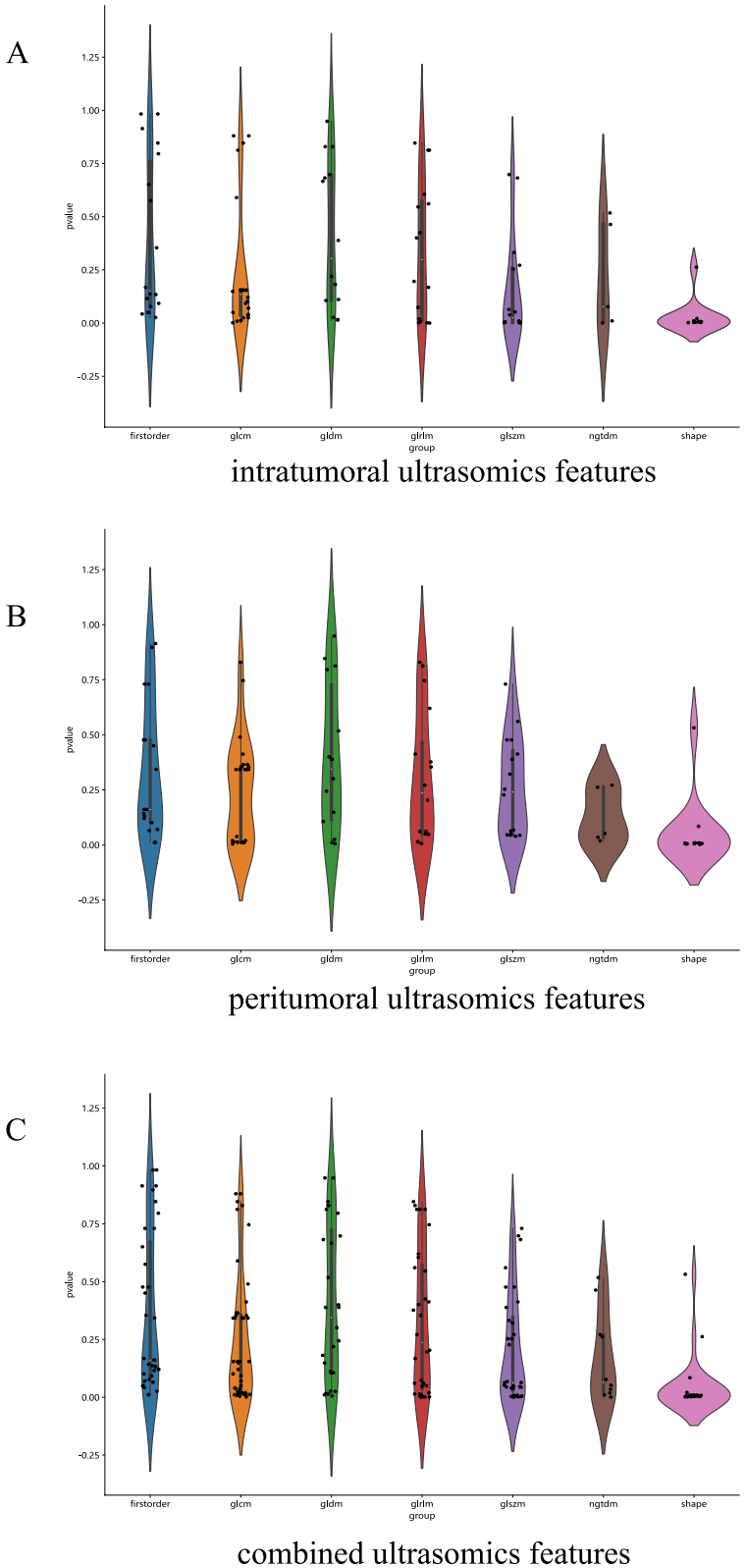

Fig. 5 Violin plot for differential analyses of intratumoral (**A**), peritumoral (**B**), and combined (**C**) ultrasomics features with their corresponding *p* values

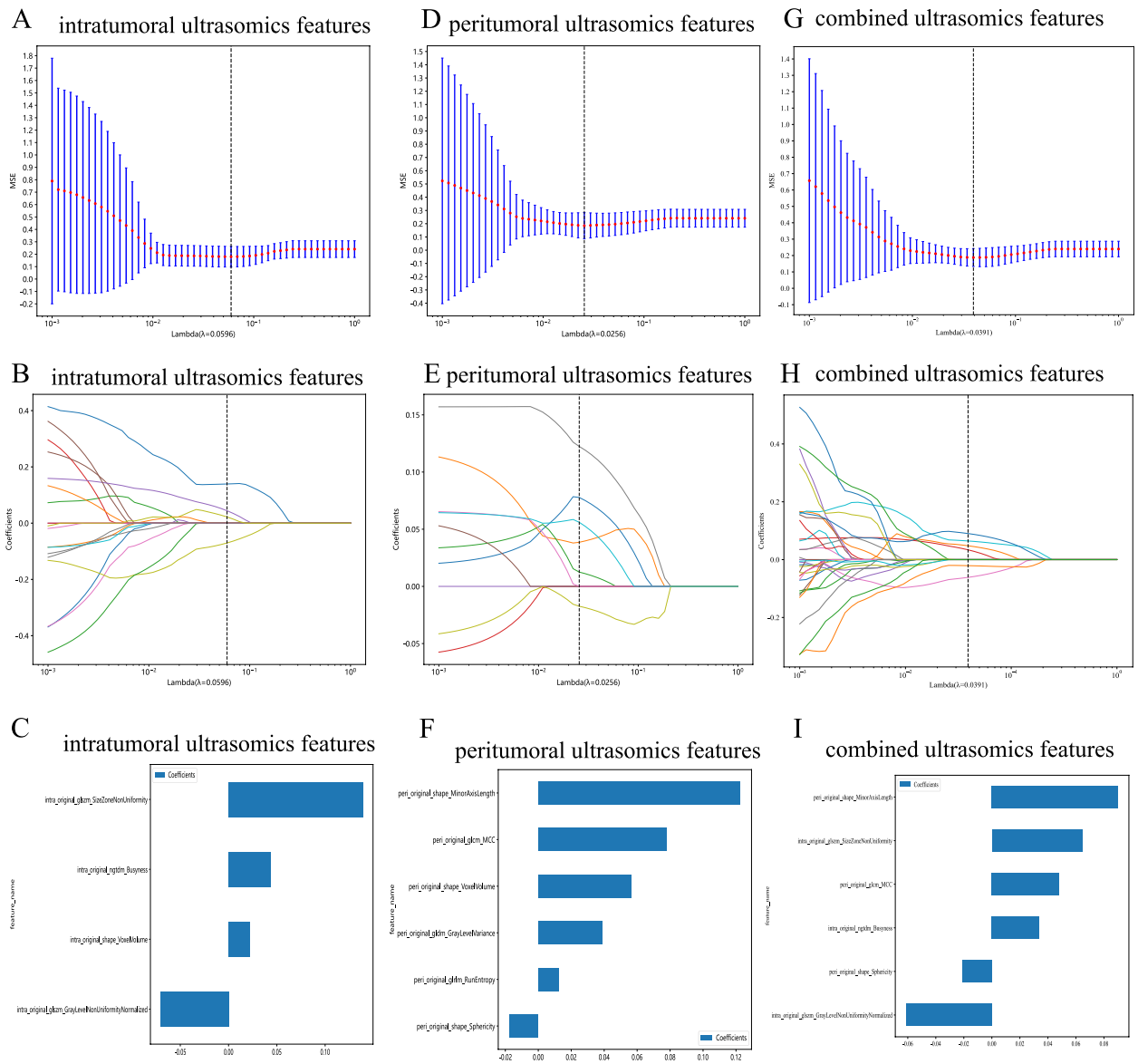

Fig. 6 Ultrasomics feature selection with the LASSO regression model. **A** The LASSO model's tuning parameter (λ) was selected using 10-fold cross-validation via the minimum criterion. The vertical lines illustrate the optimal value of the LASSO tuning parameter (λ) for the intratumoral ultrasomics features. **B** A LASSO coefficient profile plot with different log(λ) values is displayed. The vertical dashed lines represent 6 intratumoral ultrasomics features with nonzero coefficients selected with the optimal λ value. **C** The bar graph of intratumoral ultrasomics features with their nonzero coefficients. **D**, **E**, and **F** The same workflow was used for peritumoral ultrasomics feature analysis. **G**, **H**, and **I** The same workflow was used for the combined ultrasomics features analysis. ("intra" means "intratumoral"; "peri" means "peritumoral region with dilation of 3 mm")

depicted in Fig. 7A and B for the training and test groups, respectively. In both the training and test groups, the combined ultrasomics model showed the highest AUC. Detailedly, the combined ultrasomics model achieved an AUC = 0.858 (95% CI 0.7512 - 0.9642) in the training group, with an accuracy of 0.729, sensitivity of 0.765, specificity of 0.710, PPV of 0.590, and NPV of 0.765. Furthermore, in the test group, the clinical model achieved an AUC = 0.842 (95% CI 0.7061 - 0.9785) (Table 3). While the performance of these four models did not exhibit significant variances in the training group, as depicted in Fig. 7C, the combined ultrasomics model appeared to demonstrate a notable superiority over the clinical model in the test group, as illustrated in Fig. 7D, based on the results of the Delong test.

Table 3 Diagnostic performance of different models for predicting G2/3 PNETs in training and test groups

Model[a]	Cohort	AUC(95% CI)	Accuracy	Sensitivity	Specificity	PPV	NPV	F1
Combined model	Training	0.858(0.7512—0.9642)	0.729	0.765	0.710	0.591	0.765	0.667
	Test	0.842(0.7061—0.9785)	0.758	0.692	0.800	0.692	0.800	0.692
Intratumoral model	Training	0.833(0.7121—0.9540)	0.812	0.471	1.000	1.000	0.775	0.640
	Test	0.800(0.6287—0.9713)	0.788	0.692	0.850	0.750	0.810	0.720
Peritumoral model	Training	0.787(0.6440—0.9310)	0.708	0.765	0.677	0.565	0.840	0.650
	Test	0.788(0.6333—0.9436)	0.697	0.846	0.600	0.579	0.857	0.687
Clinical model	Training	0.810(0.6689—0.9516)	0.812	0.706	0.871	0.750	0.844	0.727
	Test	0.762(0.5630—0.9601)	0.788	0.692	0.850	0.750	0.810	0.720

[a] Represents models were constructed based on MLP; *MLP* Multilayer perceptron

Ultrasomics models and clinical model assessment

The calibration curves of the MLP-based various ultrasomics models and clinical model demonstrated a high level of consistency between the predicted probability and perfectly calibrated G2/3 PNETs in both the training (Fig. 8A) and test (Fig. 8B) groups. The calibration was further validated through the Hosmer-Lemeshow test, confirming the models' accurate predictions (Table 4). Additionally, DCA was conducted to assess the models' performance, with the results presented in Fig. 9. The results of the combined ultrasomics model showed a significant improvement in patient intervention efficacy in both the training (Fig. 9A) and test (Fig. 9B) groups, as evidenced by its predictive accuracy, when compared to theoretical scenarios without a prediction model, such as treating all or none. Additionally, the net benefit of the combined ultrasomics model appeared to outperform both the clinical model and other ultrasomics models in both the training and test groups.

Furthermore, the prediction accuracy of the MLP-based combined ultrasomics model was further visualized through a confusion matrix (Fig. 10A and B) and sample prediction histogram (Fig. 10C and D).

The density plot illustrated a spectrum of SHAP values for these retained feature, indicating that the model's output increased as the feature's value decreased or increased. Figures 11 and 12A demonstrates that a patient's SHAP value of 0.40 exceeds the baseline, indicating a G2/3 classification. Conversely, another patient exhibited a SHAP value of -0.73, which falls below the baseline, suggesting a G1 classification, as depicted in Fig. 12B. Therefore, the integrated ultrasomics model exhibited comparable performance in the tasks of this study.

Discussion

In contrast to surface ultrasound, EUS provides a closer and clearer view of pancreatic lesions, making it a crucial tool for evaluating pancreatic diseases [48]. Notably, preoperative EUS imaging for functional PNETs can help determine the best surgical approach by evaluating the lesion's proximity to the main pancreatic duct [49]. A significant proportion of patients with functional PNETs, often associated with multiple endocrine neoplasia type 1 (MEN1), frequently demonstrate the presence of multiple small pancreatic lesions. Given the inherent constraints of conventional CT and MRI modalities in accurately identifying these minute lesions, the use of EUS and contrast-enhanced EUS is strongly advised [33].

Numerous prior studies have examined the potential relationship between medical imaging features and the grading of PNETs. One study revealed that an indistinct boundary was more frequently observed in G2/3 PNETs with a specificity of 90.3% [22]. Additionally, Zhu H demonstrated that a well-defined margin on endoscopic ultrasound (EUS) images were predominantly linked to a lower pathological grade [28]. Claudio R also identified a positive correlation between tumor diameter and the risk of G2/3 PNETs [50]. Toshima F used univariate analysis to identify predictive factors for distinguishing between G1/2 and G3 PNETs, including tumor shape, size, and cystic degeneration. Multivariate regression analysis showed that an irregular lobulated mass was indicative of a G3 tumor diagnosis [51]. Consistent with previous findings, we found that irregular shape and larger tumor diameter were significantly associated with higher pathological grading by univariate and multivariate logistic regression analysis. Preoperative EUS imaging has demonstrated efficacy in evaluating the characteristics and proximity of functional PNETs [49]. However, the current diagnostic approach for distinguishing pancreatic masses via EUS primarily relies on macroscopic anatomical imaging features, leading to limited specificity and vulnerability to subjective interpretation by endoscopists.

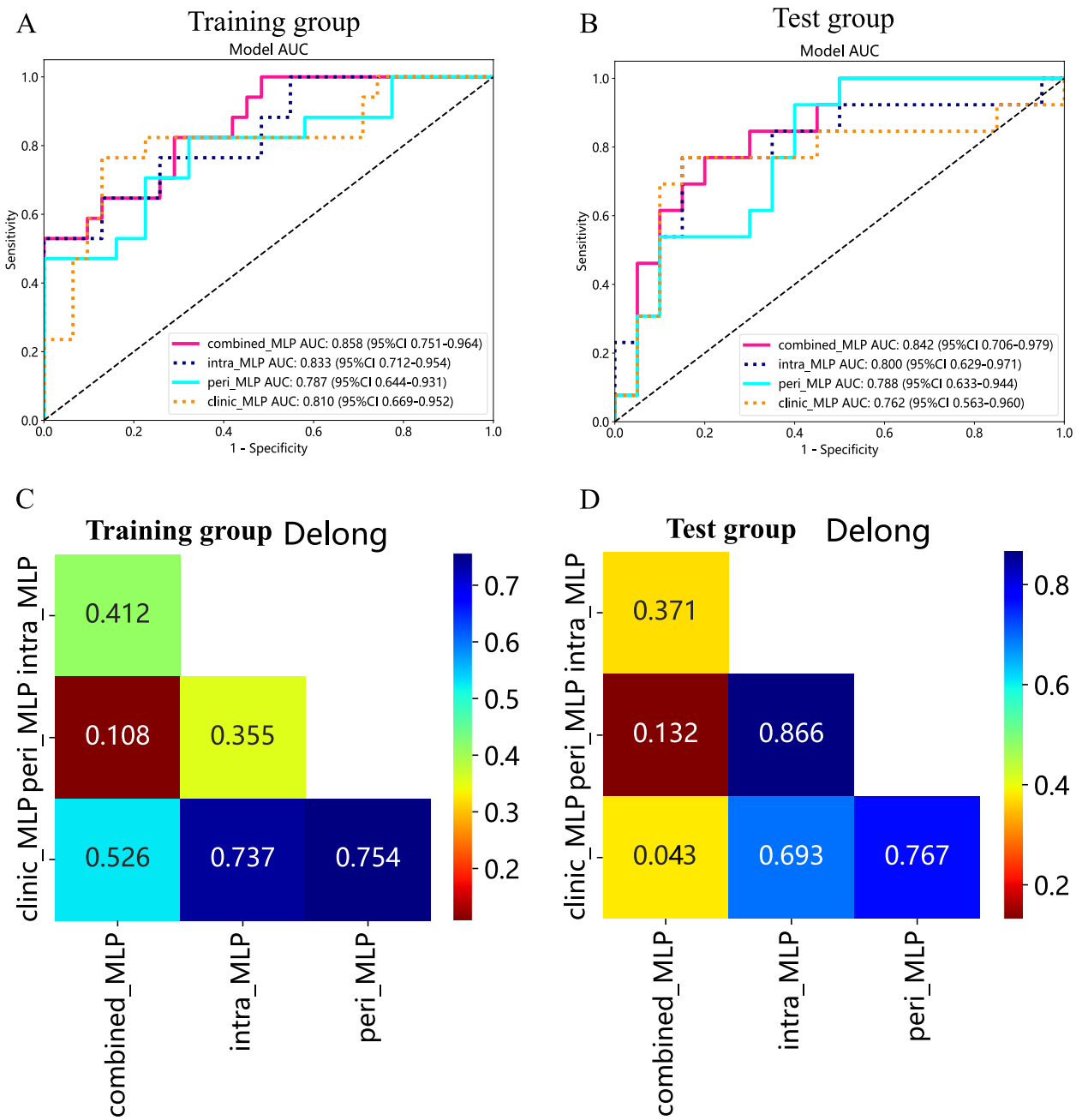

Fig. 7 The ROC curves of the different ultrasomics models and clinical models based on MLP in training (**A**) and test (**B**) groups. The results of the Delong test in the training (**C**) and test (**D**) groups. ("intra" means "intratumoral"; "peri" means "peritumoral"; clinic means "clinical")

Thus, a reliable approach that can preoperatively promote grading prediction of PNETs is an imperative need.

Radiomics enables the retrieval of multidimensional data from medical images, surpassing the limitations of human visual assessment. The utilization of radiomics can improve the effectiveness of predictive models for different tumor types, thereby enhancing the reliability and objectivity of diagnostic processes [52–54]. A multicenter study showed that non-contrast MRI radiomics and combined models outperformed clinical and radiological features in distinguishing Grade 1 and 2/3 NF-PNETs [55]. Gu D's research found that radiomic signatures from CT imaging were better at predicting the histologic grading of PNETs [30]. Similarly, the current research on endoscopic ultrasomics is also emerging.

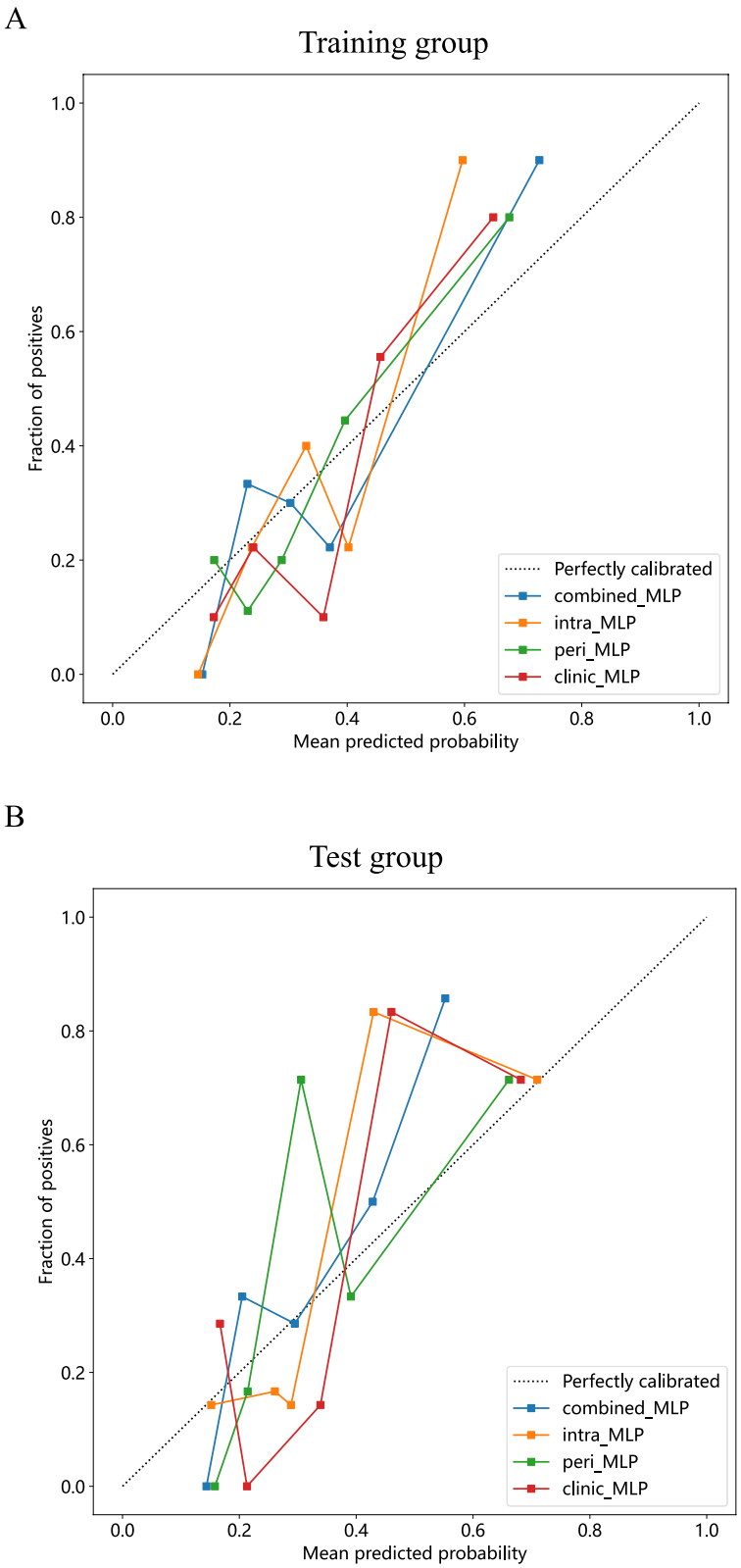

Fig. 8 The calibration curves for the different ultrasomics models and clinical models based on MLP in training (**A**) and test (**B**) groups

Table 4 The results of Hosmer-Lemeshow test

Model[a]	*P*-value	
	Training cohort	Test cohort
Intratumoral radiomics model	0.266	0.172
Peritumoral radiomics model	0.056	0.070
Clinical model	0.165	0.074
Combined radiomics model	0.424	0.209

[a] Represents models were constructed based on MLP; *MLP* Multilayer perceptron

In a multicenter study, Li XY showed that combining machine learning algorithms with EUS ultrasomics features can create a reliable classification model for assessing gastrointestinal stromal tumors (GISTs) malignancy [52]. Gu et al. developed a deep-learning ultrasomics model using EUS images to diagnose pancreatic ductal adenocarcinoma. This model effectively addresses the diagnostic variability among ultrasound endoscopy physicians with differing levels of expertise, thereby improving the accuracy of their diagnoses [56]. Similarly, a EUS-based ultrasomics model was specifically designed to differentiate between gastric GISTs, smooth muscle tumors, and nerve sheath tumors [57]. Unfortunately, there is a lack of published studies in the literature that have utilized EUS imaging ultrasomics for predicting the histologic grading of PNETs.

In this study, we utilized EUS-based ultrasomics features obtained from intratumoral ROI, along with the implementation of MLP, a machine learning algorithm, to develop predictive models for grading PNETs. The outcomes of our investigation demonstrated that the intratumoral ultrasomics model yielded remarkably accurate prediction performance for G2/3 PNETs, with an AUC of 0.833 (95% CI 0.7121-0.9540) in the training group and an AUC of 0.800 (95% CI 0.6287 - 0.9713) in the test group. The intratumoral model demonstrated comparable performance to the clinical model, which was developed using two ultrasonic features identified through multivariate logistic regression analysis. Notably, the area AUC values of the intratumoral model exceeded those of the clinical model in both the training and test groups. These results suggested that endoscopic ultrasomics might have an advantage in predicting the grading of PNETs, so we explored it further.

The current body of radiomics literature on PNETs primarily focuses on the intratumoral regions while neglecting the peritumoral region [55, 58–60]. Correspondingly, previous studies have demonstrated the significant predictive capabilities of peritumoral radiomics models concerning pathological outcomes, lymph node metastasis, and recurrence risk stratification [61–63]. Wang XX demonstrated in their study that a combined radiomic model, integrating intratumoral and peritumoral radiomics features, achieved an AUC of 0.715 (95% CI, 0.663-0.767) in the training group and 0.714 (95% CI, 0.636-0.792) in the validation group [64]. Furthermore, a similar combined model applying intratumoral and peritumoral contrast-enhancement CT radiomics features along with clinical factors was able to predict the microsatellite instability status of gastric cancer with moderate accuracy before surgery [65]. Previous studies indicated that the peritumoral area of tumors may offer important predictive and diagnostic insights. Nevertheless, the effectiveness of endoscopic ultrasound-based peritumoral ultrasomics techniques in predicting the histological grading of PNETs is currently uncertain.

Notably, in our study, the peritumoral ultrasomics model also achieved remarkably accurate prediction performance for G2/3 PNETs, with an AUC of 0.787 (95% CI, 0.6440 - 0.9310) in the training group and an AUC of 0.788 (95% CI, 0.6333 - 0.9436) in the test group. From our standpoint, both peritumoral and intratumoral regions show synergistic effects in distinguishing G1 and G2/3 PNETs. Therefore, A composite ultrasomics model incorporating characteristics from both peritumoral and intratumoral regions was developed and validated. Ultimately, this combined model performed consistently well compared to individual models, achieving an AUC of 0.858 (95% CI, 0.7512 - 0.9642) in the training group and 0.842 (95% CI, 0.7061 - 0.9785) in the test group. Furthermore, this combined ultrasomics model outperformed the clinical model in the test group. The findings, bolstered by the DeLong and H-L tests, indicate that the integrated ultrasomics model greatly improves the predictive accuracy in assessing the grading of PNETs. A prior investigation demonstrated that an ultrasomics model utilizing EUS imaging effectively distinguishes the pathological grading of PNETs, achieving an AUC of 0.987 (95%CI, 0.9650-1.0000) in the training cohort and an AUC of 0.781 (95% CI, 0.5933–0.9695) in the test cohort [66]. Nonetheless, this ultrasomics model, which exclusively concentrates on the intratumoral region, exhibits a propensity for overfitting the training data, resulting in suboptimal performance in the test cohort. In summary, the peritumoral area, specifically the tumor-adjacent parenchyma encircling the tumor lesions, provides valuable prognostic insights.

A recent study effectively employed SHAP in a CT radiomics-based model to non-invasively predict the pathological grading of PNETs [67]. In our research, we utilized SHAP values to visualize the impact of nonzero features in a combined ultrasomics model for individual patients. The summary plots underscored the significance of the retained ultrasomics features, elucidating the predicted outcomes. In addition to their high accuracy, the

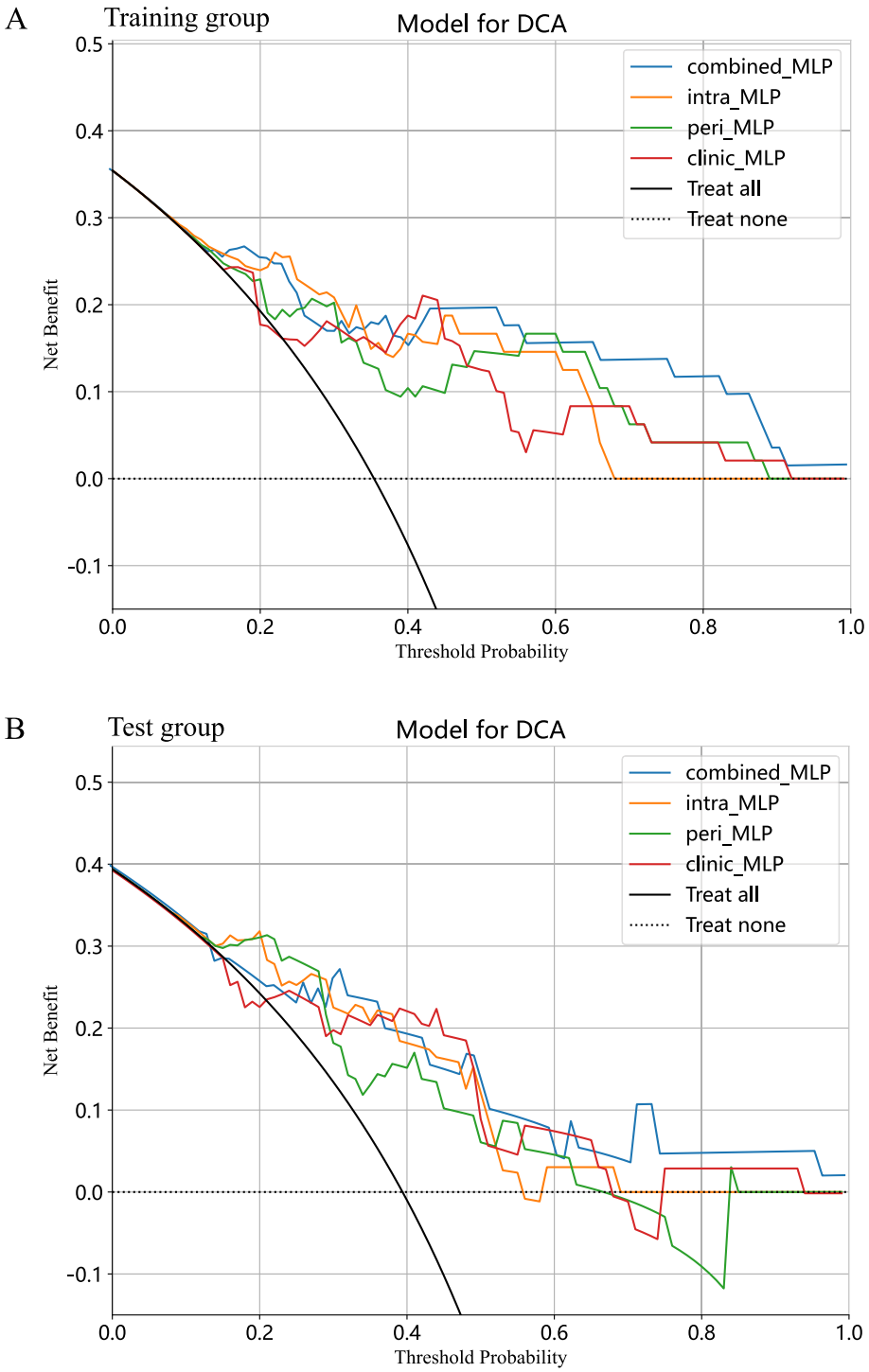

Fig. 9 The DCA curves for the different ultrasomics models and clinical models based on MLP in training (**A**) and test (**B**) groups

EUS-based combined ultrasomics models offer significant interpretability, showcasing predictive value before EUS-FNA/B and surgery.

G2/3 PNETs demonstrate a notably heightened aggressiveness compared to G1 tumors, presenting an increased susceptibility to lymph node and microvascular metastasis [68]. Moreover, metastatic PNETs display a moderate degree of T-cell infiltration when contrasted with localized PNETs [14]. Additionally, patients afflicted with G3 PNETs exhibit a significantly elevated

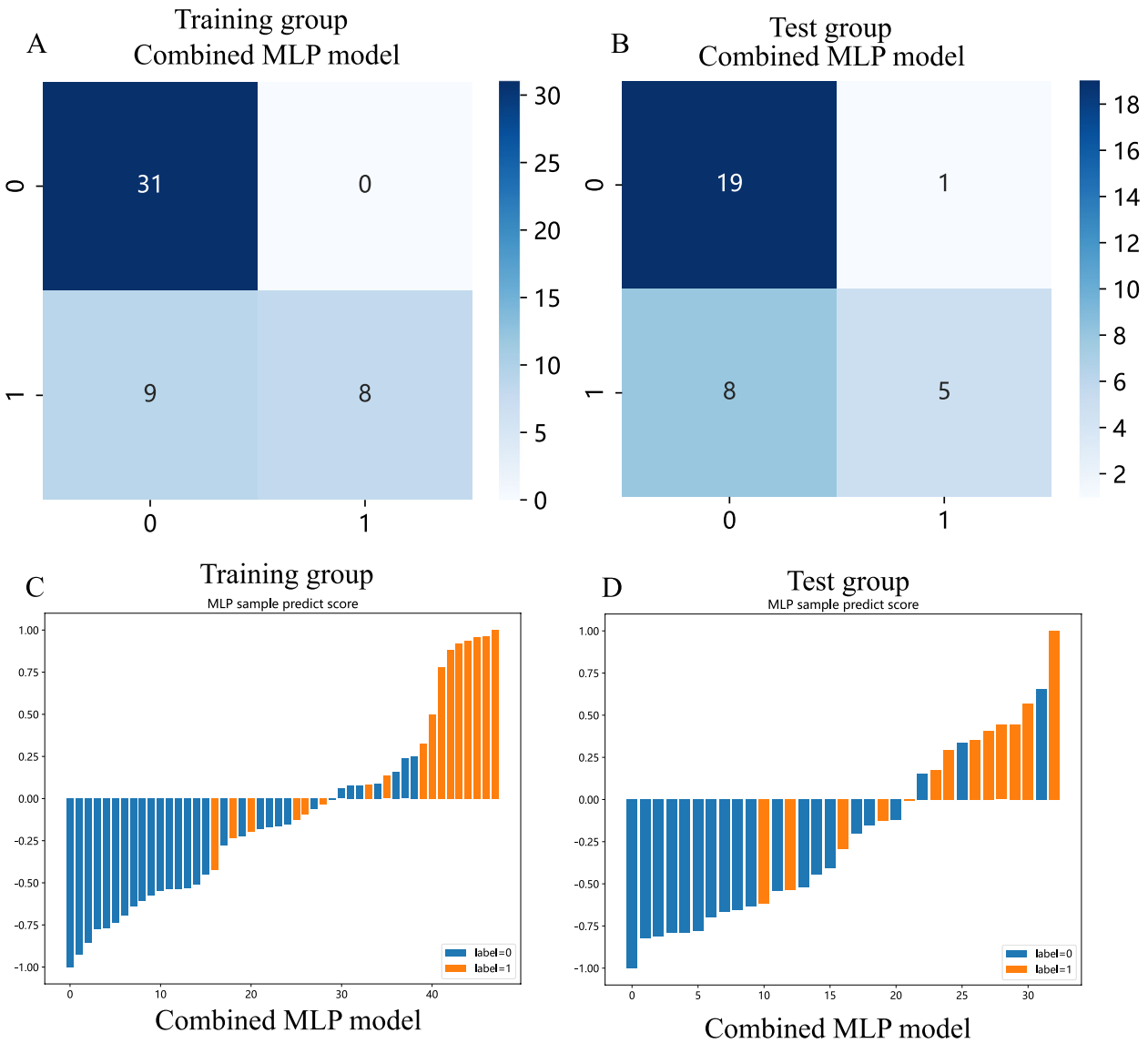

Fig. 10 **A** The confusion matrix of the combined ultrasomics model in the training group. **B** The confusion matrix of the combined ultrasomics model in the test group. **C** MLP-based prediction scores of the combined ultrasomics model in the training group. **D** MLP-based prediction scores of the combined ultrasomics model in the test group. ("label = 0" and "0" mean "G1 PNETs"; "label = 1" and "1" means "G2/3 PNETs")

neutrophil-to-lymphocyte ratio in contrast to those with G1 or G2 PNETs [69]. Prior research has demonstrated a notable association between lymphatic, microvascular, and perineural invasion (LMPI) and the prognosis of PNETs [12]. Hence, the variances in micro invasion and immune cell infiltration surrounding the tumor could potentially elucidate the disparities in the ultrasomics characteristics of EUS in the peritumoral vicinity.

In recent years, studies have demonstrated that integrating radiomics and machine learning models can enhance tumors' diagnostic, prognostic, and predictive accuracy [70, 71]. In our previous research, we presented several joint predictive models based on EUS imaging ultrasomics and machine learning algorithms, which demonstrated efficacy in distinguishing PNETs and pancreatic cancer [72], as well as differentiating between functional and non-functional PNETs [47]. These findings underscore the extensive potential of EUS ultrasomics in investigating PNETs. MLP, a feedforward network with one-way propagation and a widely employed supervised learning algorithm, is among the most common neural networks [73, 74]. Based on our results, the combined MLP models exhibited remarkable accuracy and efficiency in predicting the grading of PNETs.

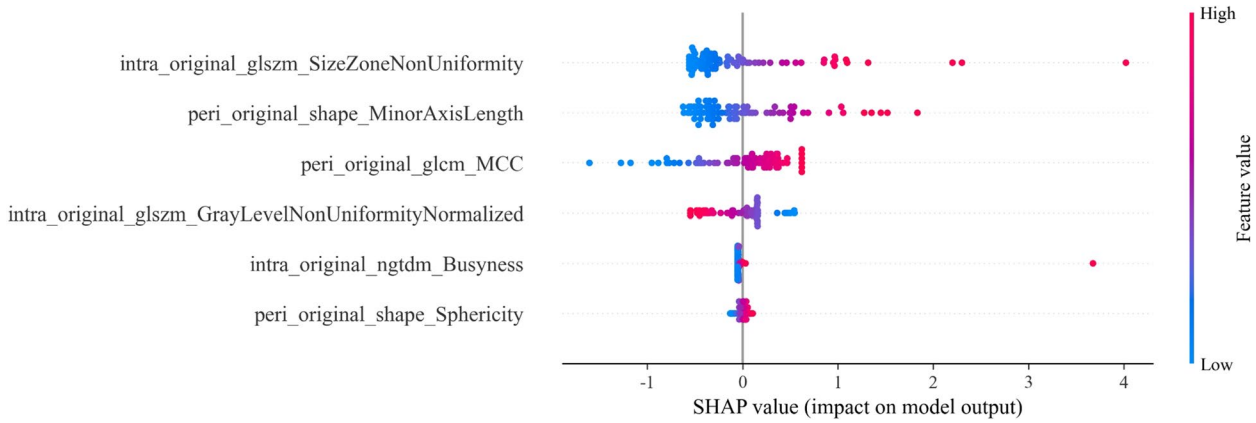

Fig. 11 SHAP summary plots of MLP-based combined model. The plot illustrated the feature relevance and combined feature attributions to the model's predictive performance

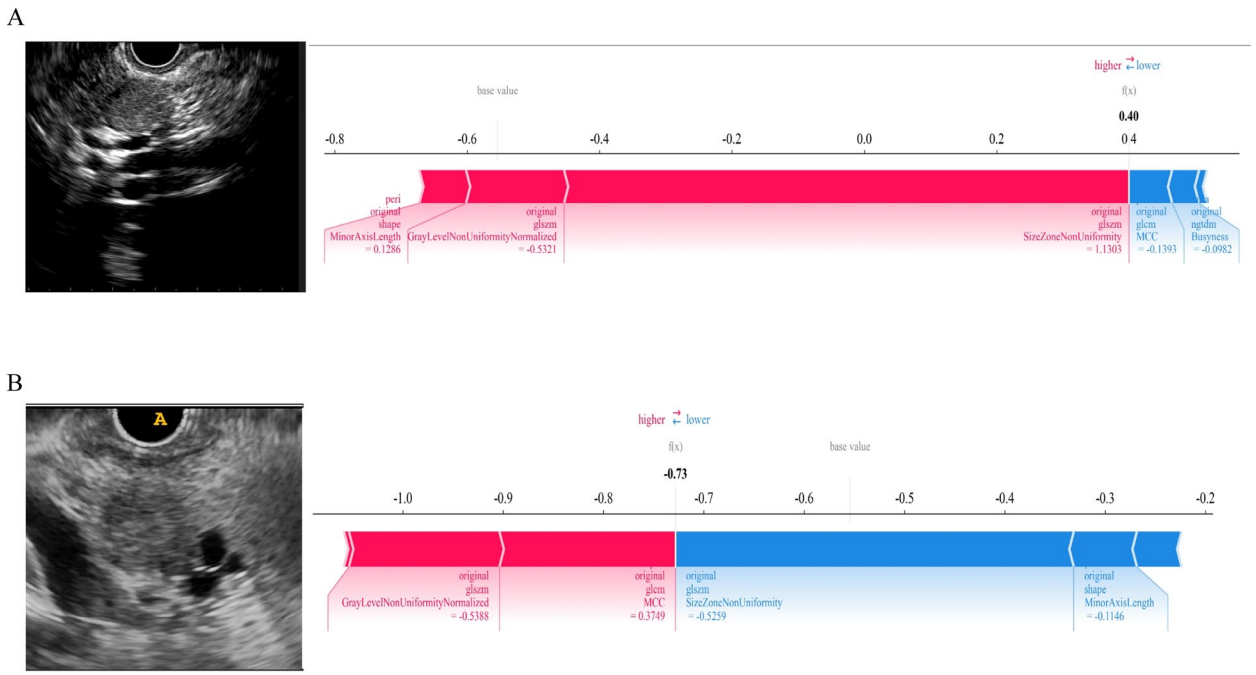

Fig. 12 SHAP force plots explain how the MLP-based combined model discriminates the pathological grading of PNETs. The predicted diagnosis of these pancreatic lesions was G2/3 (**A**) and G1 PNETs (**B**), respectively

While the ultrasomics models utilizing EUS imaging showed significant efficacy, this study is limited by several factors. Retrospective analyses performed at a single center are vulnerable to selection bias, and the manual segmentation process may introduce further bias in image segmentation [75]. The study encompassed an extended period (October 2013 to January 2024), during which advancements in imaging technology could have impacted the quality and consistency of EUS images. Consequently, future research on EUS-based ultrasomics for grading PNETs must incorporate multicenter collaborations, large sample sizes, prospective study designs, automatic delineation, and multimodal methodologies. Finally, applying deep learning techniques and studying the biological changes in peritumor imaging features could help reduce bias and enhance model interpretability.

Conclusion

In summary, a proficient ultrasomics model utilizing EUS was developed and validated, encompassing both intratumoral and peritumoral ultrasomics characteristics. The model exhibited a high level of accuracy in predicting the pathological grading of PNETs. These results present encouraging opportunities for improving the clinical efficacy of EUS and provide valuable perspectives for future investigations and implementations in this field.

Abbreviations

PNETs	Pancreatic neuroendocrine tumors
WHO	World Health Organization
CT	Computed tomography
MRI	Magnetic resonance imaging
EUS	Endoscopic ultrasonography
ENETS	European Neuroendocrine Tumor Society
US	Ultrasonography
EUS-FNA	Endoscopic ultrasonography-guided fine-needle aspiration
HU	Hounsfield units
PACS	Picture Archiving and Communication System
ROI	Region of interest
ICC	Intraclass correlation coefficient
GLCM	Gray level co-occurrence matrix
GLRLM	Gray level run length matrix
GLSZM	Gray level size zone matrix
NGTDM	Neighborhood gray-level difference matrix
IBSI	Image Biomarker Standardization Initiative
LASSO	Least absolute shrinkage and selection operator
MLP	Multilayer perceptron
ROC	Receiver operating characteristic curve
AUC	Area under the curve
PPV	Positive predictive value
NPV	Negative predictive value
H-L	Hosmer-Lemeshow
DCA	Decision curve analysis
CIC	Clinical impact curve
MSEs	Mean standard errors
CI	Confidence intervals

Supplementary Information

The online version contains supplementary material available at https://doi.org/10.1186/s12880-025-01555-x.

Supplementary Material 1.

Supplementary Material 2.

Acknowledgements

We appreciate the Onekey AI platform and its developers.

Code availability

The inquiry of the original code for this manuscript can be directed to the corresponding authors.

Authors' contributions

SM, CH , and YW designed this study and drafted the manuscript; thus, these authors contributed equally to this work and shared the first authorship. SM performed the statistical analyses. SM carried out the clinical data collection. SQ provided funding support, and these authors contributed equally to this work and shared senior authorship. All the authors contributed to the article and approved the submitted version. All the authors read and approved the final manuscript.

Funding

This study was supported by the Scientific Research Project of Liuzhou People's Hospital affiliated with Guangxi Medical University (grant numbers: lry202309 and lry202311), the Scientific Research Project of Guangxi Health Commission (grant number: Z-B20231296, Z-B20241298), and the Scientific Research Project of Liuzhou Science and Technology Bureau (grant number:2024YB0101B005,2024SB0104C009). The funding bodies played no role in the design of the study and collection, analysis, and interpretation of data and in writing the manuscript.

Data availability

The original data presented in the study are included in the article/Supplementary Material; further inquiries can be directed to the corresponding authors.

Declarations

Ethics approval and consent to participate

This retrospective study was approved by the Medical Ethics Committee of The First Affiliated Hospital of Guangxi Medical University (No. 2023-K346-01, 2023-12-29) and conformed to the Declaration of Helsinki. Informed consent was obtained from all subjects and/or their legal guardians.

Consent for publication

Not applicable.

Competing interests

The authors declare no competing interests.

Author details

[1]Gastroenterology Department/Clinical Nutrition Department, Liuzhou People's Hospital Affiliated to Guangxi Medical University, Liuzhou, China. [2]Gastroenterology Department, The First Affiliated Hospital of Guangxi Medical University, Nanning, China. [3]Oncology Department, Liuzhou Peoples' Hospital Affiliated to Guangxi Medical University, Liuzhou, China.

Received: 25 March 2024 Accepted: 3 January 2025
Published online: 18 January 2025

References

1. Hu Y, et al. Role of somatostatin receptor in pancreatic neuroendocrine tumor development, diagnosis, and therapy. Front Endocrinol. 2021;12:679000.
2. April-Monn SL, et al. EZH2 inhibition as new epigenetic treatment option for pancreatic neuroendocrine neoplasms (PanNENs). Cancers. 2021;13(19):5014.
3. Partouche E, et al. Updated trends in imaging practices for pancreatic neuroendocrine tumors (PNETs): a systematic review and meta-analysis to pave the way for standardization in the new era of big data and artificial intelligence. Front Oncol. 2021;11:628408.
4. Gollapudi LA, Tyberg A. EUS-RFA of the pancreas: where are we and future directions. Transl Gastroenterol Hepatol. 2022;7:18.
5. Buchstab O, Knösel T. Current WHO classification (2022) of neuroendocrine neoplasms. Radiologie (Heidelberg, Germany). 2024;64(7):531–5.
6. D'Onofrio M, et al. CT enhancement and 3D texture analysis of pancreatic neuroendocrine neoplasms. Sci Rep. 2019;9:2176.
7. Zhang R, et al. Novel staging for gastric neuroendocrine neoplasms by incorporating the WHO grading into the TNM staging system. Cancer Med. 2023;12:6623–36.
8. Tong Z, et al. Clonal evolution dynamics in primary and metastatic lesions of pancreatic neuroendocrine neoplasms. Front Med. 2021;8:620988.
9. Partelli S, et al. Management of asymptomatic sporadic nonfunctioning pancreatic neuroendocrine neoplasms (ASPEN) ≤2 cm: study protocol for a prospective observational study. Front Med. 2020;7:598438.
10. Sadowski SM, Pieterman CRC, Perrier ND, Triponez F, Valk GD. Prognostic factors for the outcome of nonfunctioning pancreatic neuroendocrine tumors in MEN1: a systematic review of literature. Endocr Relat Cancer. 2020;27:R145-r161.

11. Liang W, et al. A combined nomogram model to preoperatively predict histologic grade in pancreatic neuroendocrine tumors. Clin Cancer Res: an official journal of the American Association for Cancer Research. 2019;25:584–94.
12. Liu YL, et al. Prediction of the lymphatic, microvascular, and perineural invasion of pancreatic neuroendocrine tumors using preoperative magnetic resonance imaging. World J Gastrointest Surg. 2023;15:2809–19.
13. Zhu HB, et al. Radiomics analysis from magnetic resonance imaging in predicting the grade of nonfunctioning pancreatic neuroendocrine tumors: a multicenter study. Eur Radiol. 2024;34:90–102.
14. Greenberg J, et al. Metastatic pancreatic neuroendocrine tumors feature elevated T cell infiltration. JCI insight. 2022;7(23):e160130.
15. Osher E, et al. A lymph node ratio model for prognosis of patients with pancreatic neuroendocrine tumors. Biomedicines. 2023;11(2):407.
16. Yang DH, et al. Prediction of pathological grades of pancreatic neuroendocrine tumors based on dynamic contrast-enhanced ultrasound quantitative analysis. Diagnostics (Basel, Switzerland). 2023;13(2):238.
17. Pulvirenti A, et al. Quantitative computed tomography image analysis to predict pancreatic neuroendocrine tumor grade. JCO Clin Cancer Inform. 2021;5:679–94.
18. Hedenström P. The best approach for sampling of pancreatic neuroendocrine tumors - EUS-FNA or EUS-FNB? Endosc Int Open. 2019;7:E1400-e1402.
19. Appelstrand A, Bergstedt F, Elf AK, Fagman H, Hedenström P. Endoscopic ultrasound-guided side-fenestrated needle biopsy sampling is sensitive for pancreatic neuroendocrine tumors but inadequate for tumor grading: a prospective study. Sci Rep. 2022;12:5971.
20. Grosse C, Noack P, Silye R. Accuracy of grading pancreatic neuroendocrine neoplasms with Ki-67 index in fine-needle aspiration cellblock material. Cytopathology : official journal of the British Society for Clinical Cytology. 2019;30:187–93.
21. Paiella S, et al. Endoscopic ultrasound-guided fine-needle aspiration for the diagnosis and grading of pancreatic neuroendocrine tumors: a retrospective analysis of 110 cases. Endoscopy. 2020;52:988–94.
22. De Robertis R, et al. Pancreatic neuroendocrine neoplasms: magnetic resonance imaging features according to grade and stage. World J Gastroenterol. 2017;23:275–85.
23. Jang KM, Kim SH, Lee SJ, Choi D. The value of gadoxetic acid-enhanced and diffusion-weighted MRI for prediction of grading of pancreatic neuroendocrine tumors. Acta Radiol (Stockholm, Sweden : 1987). 2014;55:140–8.
24. Belousova E, et al. Contrast-enhanced MDCT in patients with pancreatic neuroendocrine tumours: correlation with histological findings and diagnostic performance in differentiation between tumour grades. Clin Radiol. 2017;72:150–8.
25. Canellas R, Burk KS, Parakh A, Sahani DV. Prediction of pancreatic neuroendocrine tumor grade based on CT features and texture analysis. AJR Am J Roentgenol. 2018;210:341–6.
26. Kang J, et al. Association between pathologic grade and multiphase computed tomography enhancement in pancreatic neuroendocrine neoplasm. J Gastroenterol Hepatol. 2018. https://doi.org/10.1111/jgh.14139.
27. De Robertis R, et al. Can histogram analysis of MR images predict aggressiveness in pancreatic neuroendocrine tumors? Eur Radiol. 2018;28:2582–91.
28. Zhu H, Ying L, Tang W, Yang X, Sun B. Can MDCT or EUS features predict the histopathological grading scheme of pancreatic neuroendocrine neoplasms? Radiol Med (Torino). 2017;122:319–26.
29. Franchellucci G, et al. Contrast enhanced EUS for predicting solid pancreatic neuroendocrine tumor grade and aggressiveness. Diagnostics (Basel, Switzerland). 2023;13(2):239.
30. Gu D, et al. CT radiomics may predict the grade of pancreatic neuroendocrine tumors: a multicenter study. Eur Radiol. 2019;29:6880–90.
31. Melita G, et al. Diagnostic and interventional role of endoscopic ultrasonography for the management of pancreatic neuroendocrine neoplasms. J Clin Med. 2021;10(12):2638.
32. Hofland J, et al. European Neuroendocrine Tumor Society 2023 guidance paper for functioning pancreatic neuroendocrine tumour syndromes. J Neuroendocrinol. 2023;35: e13318.
33. Costache MI, et al. Clinical impact of strain histogram EUS elastography and contrast-enhanced EUS for the differential diagnosis of focal pancreatic masses: a prospective multicentric study. Endosc Ultrasound. 2020;9:116–21.
34. Kann PH. Is endoscopic ultrasonography more sensitive than magnetic resonance imaging in detecting and localizing pancreatic neuroendocrine tumors? Rev Endocr Metab Disord. 2018;19:133–7.
35. Iqbal J, et al. Reimagining healthcare: unleashing the power of artificial intelligence in medicine. Cureus. 2023;15:e44658.
36. Huang AA, Huang SY. Increasing transparency in machine learning through bootstrap simulation and shapely additive explanations. PLoS One. 2023;18:e0281922.
37. Tong P, Sun D, Chen G, Ni J, Li Y. Biparametric magnetic resonance imaging-based radiomics features for prediction of lymphovascular invasion in rectal cancer. BMC Cancer. 2023;23:61.
38. Wang X, et al. Development of the prediction model based on clinical-imaging omics: molecular typing and sentinel lymph node metastasis of breast cancer. Ann Transl Med. 2022;10:749.
39. Hashido T, Saito S, Ishida T. A radiomics-based comparative study on arterial spin labeling and dynamic susceptibility contrast perfusion-weighted imaging in gliomas. Sci Rep. 2020;10:6121.
40. Bian Y, et al. Noncontrast radiomics approach for predicting grades of nonfunctional pancreatic neuroendocrine tumors. J Magn Reson Imaging : JMRI. 2020;52:1124–36.
41. Guo CG, et al. Pancreatic neuroendocrine tumor: prediction of the tumor grade using magnetic resonance imaging findings and texture analysis with 3-T magnetic resonance. Cancer Manag Res. 2019;11:1933–44.
42. Ye JY, et al. A radiomics-based interpretable model to predict the pathological grade of pancreatic neuroendocrine tumors. Eur Radiol. 2024;34(3):1994–2005.
43. Dong Y, et al. Pancreatic neuroendocrine tumor: prediction of tumor grades by radiomics models based on ultrasound images. Br J Radiol. 2023;96:20220783.
44. Du N, et al. An initial study on the predictive value using multiple MRI characteristics for Ki-67 labeling index in glioma. J Transl Med. 2023;21:119.
45. Zhuo Y, et al. Radiomics nomograms of tumors and peritumoral regions for the preoperative prediction of spread through air spaces in lung adenocarcinoma. Transl Oncol. 2020;13:100820.
46. Pérez-Morales J, et al. Peritumoral and intratumoral radiomic features predict survival outcomes among patients diagnosed in lung cancer screening. Sci Rep. 2020;10:10528.
47. Mo S, et al. Endoscopic ultrasonography-based intratumoral and peritumoral machine learning radiomics analyses for distinguishing insulinomas from non-functional pancreatic neuroendocrine tumors. Front Endocrinol. 2024;15:1383814.
48. Facciorusso A, et al. Needle tract seeding after endoscopic ultrasound tissue acquisition of pancreatic lesions: a systematic review and meta-analysis. Diagnostics (Basel, Switzerland). 2022;12(9):2113.
49. Giuliani T, et al. Endoscopic placement of pancreatic stent for "Deep" pancreatic enucleations operative technique and preliminary experience at two high-volume centers. Surg Endosc. 2020;34:2796–802.
50. Ricci C, et al. The 3-dimensional-computed tomography texture is useful to predict pancreatic neuroendocrine tumor grading. Pancreas. 2021;50:1392–9.
51. Toshima F, et al. Is the combination of MR and CT findings useful in determining the tumor grade of pancreatic neuroendocrine tumors? Jpn J Radiol. 2017;35:242–53.
52. Li X, Jiang F, Guo Y, Jin Z, Wang Y. Computer-aided diagnosis of gastrointestinal stromal tumors: a radiomics method on endoscopic ultrasound image. Int J Comput Assist Radiol Surg. 2019;14:1635–45.
53. Geng X, et al. Radiomics-clinical nomogram for preoperative lymph node metastasis prediction in esophageal carcinoma. Br J Radiol. 2024;97(1155):652–9.
54. Bezzi C, et al. Radiomics in pancreatic neuroendocrine tumors: methodological issues and clinical significance. Eur J Nucl Med Mol Imaging. 2021;48:4002–15.
55. Zhu HB, et al. Radiomics analysis from magnetic resonance imaging in predicting the grade of nonfunctioning pancreatic neuroendocrine tumors: a multicenter study. Eur Radiol. 2024;34(1):90–102.
56. Gu J, et al. Prospective assessment of pancreatic ductal adenocarcinoma diagnosis from endoscopic ultrasonography images with the assistance of deep learning. Cancer. 2023;129:2214–23.

57. Zhang XD, et al. A combined radiomic model distinguishing GISTs from leiomyomas and schwannomas in the stomach based on endoscopic ultrasonography images. J Appl Clin Med Phys. 2023;24: e14023.
58. Bian Y, et al. Magnetic resonance imaging radiomic analysis can preoperatively predict G1 and G2/3 grades in patients with NF-pNETs. Abdom Radiol (New York). 2021;46:667–80.
59. Benedetti G, et al. CT-derived radiomic features to discriminate histologic characteristics of pancreatic neuroendocrine tumors. Radiol Med (Torino). 2021;126:745–60.
60. Mori M, et al. Ct radiomic features of pancreatic neuroendocrine neoplasms (panNEN) are robust against delineation uncertainty. Phys Med: PM : an international journal devoted to the applications of physics to medicine and biology : official journal of the Italian Association of Biomedical Physics (AIFB). 2019;57:41–6.
61. Xie N, et al. Peritumoral and intratumoral texture features based on multiparametric MRI and multiple machine learning methods to preoperatively evaluate the pathological outcomes of pancreatic cancer. J Magn Reson Imaging : JMRI. 2023;58:379–91.
62. Shi J, et al. MRI-based peritumoral radiomics analysis for preoperative prediction of lymph node metastasis in early-stage cervical cancer: A multi-center study. Magn Reson Imaging. 2022;88:1–8.
63. Sun Q, et al. Deep learning vs. radiomics for predicting axillary lymph node metastasis of breast cancer using ultrasound images: don't forget the peritumoral region. Front Oncol. 2020;10:53.
64. Wang XX, et al. Intratumoral and peritumoral radiomics analysis for preoperative Lauren classification in gastric cancer. Cancer Imaging : the official publication of the International Cancer Imaging Society. 2020;20:83.
65. Chen X, et al. Intratumoral and peritumoral CT-based radiomics for predicting the microsatellite instability in gastric cancer. Abdom Radiol (New York). 2024;49(5):1363–75.
66. Mo S, Wang Y, Huang C, Wu W, Qin S. A novel endoscopic ultrasomics-based machine learning model and nomogram to predict the pathological grading of pancreatic neuroendocrine tumors. Heliyon. 2024;10: e34344.
67. Ye JY, et al. A radiomics-based interpretable model to predict the pathological grade of pancreatic neuroendocrine tumors. Eur Radiol. 2024;34:1994–2005.
68. Molasy B, Zemła P, Mrowiec S, Grudzińska E, Kuśnierz K. Evaluation of risk factors for distant and lymph node metastasis of pancreatic neuroendocrine tumors. Ther Clin Risk Manag. 2022;18:745–52.
69. Oh D, Pyo JS, Chung KH, Son BK. The predicting role of the neutrophil-to-lymphocyte ratio for the tumor grade and prognosis in pancreatic neuroendocrine tumors. Diagnostics (Basel, Switzerland). 2022;12(3):737.
70. Wan S, et al. CT-based machine learning radiomics predicts CCR5 expression level and survival in ovarian cancer. J Ovarian Res. 2023;16:1.
71. Yan C, et al. Machine learning-based combined nomogram for predicting the risk of pulmonary invasive fungal infection in severely immunocompromised patients. Ann Transl Med. 2022;10:514.
72. Mo S, et al. Construction and validation of an endoscopic ultrasonography-based ultrasomics nomogram for differentiating pancreatic neuroendocrine tumors from pancreatic cancer. Front Oncol. 2024;14:1359364.
73. Ren R, Su J, Yang B, Lau RYK, Liu Q. Novel low-power construction of chaotic S-box in multilayer perceptron. Entropy (Basel, Switzerland). 2022;24.
74. Alnuaim AA, et al. Human-computer interaction for recognizing speech emotions using multilayer perceptron classifier. J Healthc Eng. 2022;2022:6005446.
75. Lohmann P, Bousabarah K, Hoevels M, Treuer H. Radiomics in radiation oncology-basics, methods, and limitations. Strahlentherapie und Onkologie : Organ der Deutschen Rontgengesellschaft ... [et al]. 2020;196:848–855.

Publisher's Note